Cell-Vertex Adaptive Euler Method for Cascade Flows

L. A. Catalano,* P. De Palma,* M. Napolitano,† and G. Pascazio*
Politecnico di Bari, 70125 Bari, Italy

This paper is concerned with the numerical solution of the two-dimensional steady Euler equations, using a multidimensional upwind cell-vertex residual distribution scheme. A solution-adaptive grid-refinement procedure is proposed, which combines with an efficient multigrid strategy based on an optimally smoothing explicit multistage scheme. A very accurate treatment of solid wall boundaries and a general approach for guaranteeing conservation on patched grids are developed within the present context of cell-vertex residual distribution schemes. The proposed approach is shown to be very efficient and sufficiently accurate to compute the transonic flow past a high-turning turbine cascade.

I. Introduction

IN the last few years, a large effort has been devoted to the development of numerical methods for solving the multidimensional Euler equations with improved discontinuity-capturing capability. Classical upwind methods, based on the application of one-dimensional Riemann solvers along grid dependent directions, experience a loss of resolution in the presence of discontinuities not aligned with the mesh. In order to overcome such a difficulty, two different approaches have been proposed that introduce a truly multidimensional modeling of the propagation phenomena dominating the behavior of compressible flows. The Euler system is decomposed either into an equivalent set of five-to-six simple wave equations[1] or into a system of four optimally decoupled compatibility equations.[2] The scalar equations are solved using one of the newly developed multidimensional fluctuation splitting (FS) space discretization schemes,[3] that send the residual calculated over each cell-vertex triangular element to its downstream nodes. The more robust methodology introduced by Roe[1] and further developed in Refs. 4–6 has been widely used by the authors in combination with the linear first-order accurate space discretization *N*-scheme.[3] A standard full approximation scheme (FAS) multigrid strategy with an optimally smoothing explicit three-stage scheme[5–7] has been employed to obtain a very efficient genuinely multidimensional Euler solver. The compact space discretization and the explicit time integration make the resulting methodology ideally suited for adaptive mesh refinement as well as for vector and parallel computers. In particular, the use of a solution-adaptive grid-refinement strategy is expected to further improve the efficiency of the method, as well as to make it sufficiently accurate for computing two-dimensional complex Euler flows.

In this paper, after reviewing the basic multidimensional upwind FS Euler solver, a multigrid adaptive strategy is proposed that effectively combines a solution-adaptive grid-refinement procedure with the FAS multigrid approach based on the optimally smoothing explicit scheme.[6,7] Furthermore, the solid wall boundary conditions based on isentropic simple radial equilibrium (ISRE)[8] are generalized to the present context of cell-vertex distribution schemes, and a general approach for guaranteeing conservation on patched grids is developed. Finally, results are presented for two transonic cascade flows. A simple cascade of NACA 0012 airfoils is used to demonstrate the accuracy improvement obtained using the ISRE wall boundary conditions with respect to the standard characteristic ones. A severe high-turning turbine blade cascade is employed to

validate the patched-grid treatment as well as the solution-adaptive grid-refinement procedure.

II. Euler Solver

The governing equations for inviscid nonconducting flows are written in terms of the conservative variables, $q = (\rho, \rho u, \rho v, \rho E)^T$, as

$$q_t = -\nabla \cdot \mathcal{F} = \text{res}(q), \qquad \mathcal{F} = (F, G) \qquad (1)$$

where $F = (\rho u, \rho u^2 + p, \rho u v, \rho u H)^T$ and $G = (\rho v, \rho u v, \rho v^2 + p, \rho v H)^T$ are the flux vectors in the x and y directions, respectively.

The present numerical method is based on the application of simple-wave theory to the Euler equations (1) (see Ref. 1) and consists in selecting a number N of waves (acoustic, entropy, shear), each having strength α^k and propagation direction n^k. In this way 1) the gradient of the primitive variables $\tilde{q} = (\rho, u, v, p)^T$ can be decomposed as

$$\nabla \tilde{q} = \sum_{k=1}^{N} \nabla \tilde{q}^k = \sum_{k=1}^{N} \alpha^k \tilde{r}^k n^k \qquad (2)$$

where $\tilde{r}^k$ is the right eigenvector of the Jacobian $(\partial F/\partial \tilde{q}' n_x^k + \partial G/\partial \tilde{q} n_y^k)$ with eigenvalue λ^k, and 2) the time derivative of the conservative variables can be obtained by summing up all wave contributions, as follows[1]:

$$q_t = -\sum_{k=1}^{N} \alpha^k r^k \lambda^k = \text{res}(q) \qquad (3)$$

An analytical decomposition can be obtained when employing four orthogonal acoustic waves, one entropy wave, and one shear wave.[1] Depending on the flow data, $\nabla \tilde{q}$, the intensities of all waves and the propagation directions of the acoustic and entropy waves are provided by Eq. (2), whereas the direction of the shear remains arbitrary. Several models have been proposed that differ on the choice of this direction.[1,4,5,9] The model employing a shear propagating along the streamline, as proposed in Ref. 5, has proven robust for a wide range of applications and is employed in the present paper.

A cell-vertex triangular discretization appears to be the most suitable choice for a wave decomposition model based on the gradients of the flow variables. For each triangle T, the global fluctuation, defined as $\Phi_T = \int_{S_T} q_t \, dS$, is split into its simple-wave contributions as follows:

$$\Phi_T = -\int_{S_T} \sum_{k=1}^{N} \alpha^k r^k \lambda^k \, dS = -S_T \sum_{k=1}^{N} \bar{\alpha}^k \bar{r}^k \bar{\lambda}^k = \sum_{k=1}^{N} \Phi_T^k \qquad (4)$$

In Eq. (4), the cell-averaged values $\bar{\alpha}^k$, $\bar{r}^k$, and $\bar{\lambda}^k$ can be evaluated analytically, provided that the parameter vector $z = \sqrt{(\rho)}(1, u, v, H)^T$ is assumed to vary bilinearly over each triangle, a feature that is crucial to ensure conservation.[10] Each wave

contribution to the flux balance Φ_T^k is then split among the vertices of the triangle, according to the compact-stencil FS approach.[3] The discrete residual of Eq. (1) at each vertex v can thus be written as

$$(q_t)_v = \mathrm{res}_v(q) = \frac{1}{S_v} \sum_T \sum_{k=1}^N \beta_{T,v}^k \Phi_T^k \qquad (5)$$

In Eq. (5), $\beta_{T,v}^k$ are the coefficients that define the contribution of the kth wave component to the vertex v of the triangle T; the area S_v is only a suitable scale factor in the case of steady-state calculations, and the summation is extended over all triangles having the vertex v in common. Obviously, in order to ensure conservation, for every triangle T and for each wave k, the following condition must be satisfied:

$$\sum_{j=1}^3 \beta_{T,j}^k = 1 \qquad (6)$$

In the present paper, the $\beta_{T,j}^k$ coefficients employed are the ones corresponding to the first-order accurate FS N-scheme.[3]

III. Multigrid Adaptive Strategy

To combine the basic solver with the quad-tree data structure used to create locally refined grids,[11] the triangular mesh is obtained from a structured quadrilateral one. The standard FAS multigrid V cycle[12] using full-weighting collection and bilinear prolongation is employed in combination with an optimally smoothing multi stage Runge–Kutta scheme, designed using a two-dimensional linear Fourier analysis.[5-7]

The use of a spatial discretization based on compact stencils and the choice of an explicit time-stepping scheme as smoother make the basic solver very suitable for grid adaptivity, an essential feature for addressing complex flow situations. A solution-adaptive local-refinement strategy for cell-vertex residual distribution methods is developed and applied to the decomposition method described in the preceding section: starting from a regular structured quadrilateral grid, nested levels of local refinement are created and managed by a quad-tree data structure.[11] At each level l, the grid Ω^l is composed of an unrefined part Ω_c^l (cells with no kids) and of a refined one Ω_f^l (cells with kids on the level $l + 1$), so that Ω_f^l and Ω^{l+1} cover the same region. In such a way, the physical domain is discretized by a grid composed of all unrefined parts Ω_c^l, $l = 0, \ldots, N$ (composite grid with N levels of local refinement). To describe how the conservation property of the basic solver is maintained over the composite grid, two nested levels, l and $l + 1$, are considered; see Fig. 1: the boundary points of Ω^{l+1} that do not lie on the physical boundary, called green nodes, are denoted by crosses, whereas the dots indicate the interior nodes of Ω^{l+1}. The solution at level $l + 1$ is firstly obtained by bilinear interpolation of the solution at level l, as done in the standard nested iteration; the FS scheme, namely, Eqs. (4) and (5), is then applied on the grid $l + 1$ to reconstruct the residual at all interior nodes; only incomplete contributions are sent to the green nodes, which therefore are not updated in the time integration. In order to apply the coarse grid correction, the solution is then injected from the level $l + 1$ to the level l, namely,

$$q_{i,j}^l = q_{2i,2j}^{l+1} \qquad (7)$$

A first condition to be satisfied for ensuring conservation on the composite grid is that the flux through each side of $\partial\Omega_f^l$ coincides with the flux through the two corresponding sides on $\partial\Omega^{l+1}$ exactly or within its local order of accuracy. For the present linear-element cell-vertex discretization, the latter requirement is clearly satisfied when using bilinear interpolation of either the primitive or the conservative variables at green nodes. Furthermore, thanks to the analytical linearization, the flux can be conserved exactly by interpolating the parameter vector, which has already been supposed to vary bilinearly over each cell. Integrating along $\partial\Omega_f^l$ and $\partial\Omega^{l+1}$, one has

$$\oint_{\partial\Omega^{l+1}} \mathcal{F} \cdot n \, ds - \oint_{\partial\Omega_f^l} \mathcal{F} \cdot n \, ds = 0 \quad \text{or} \quad \mathcal{O}(h^2) \qquad (8)$$
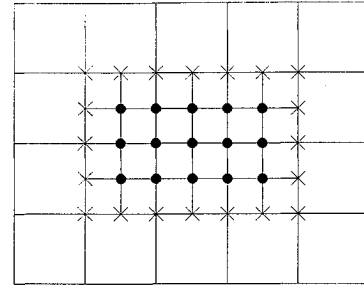

Fig. 1   Interior and green nodes on a composite grid.
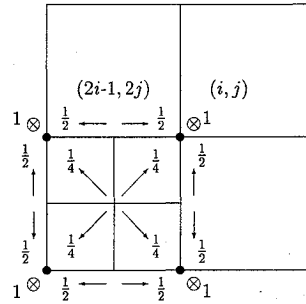

Fig. 2   Residual collection on the composite grid.

where n is the outward normal. Using Gauss' theorem, Eq. (8) reads

$$\int_{\Omega^{l+1}} \nabla \cdot \mathcal{F} dS - \int_{\Omega_f^l} \nabla \cdot \mathcal{F} dS = 0 \quad \text{or} \quad \mathcal{O}(h^2) \qquad (9)$$

In the discrete domain, Eq. (9) can be rewritten in terms of the contributions received by each node as

$$\sum_{v \in \Omega^{l+1}} R_v^{\Omega^{l+1}} - \sum_{v \in \Omega_f^l} R_v^{\Omega_f^l} = 0 \quad \text{or} \quad \mathcal{O}(h^2) \qquad (10)$$

the argument of each summation being defined as

$$R_v^{\hat{\Omega}} = \sum_{T \in \hat{\Omega}} \sum_{k=1}^N \beta_{T,v}^k \Phi_T^k, \qquad \forall \hat{\Omega}, \qquad \forall v \in \hat{\Omega} \qquad (11)$$

In Eq. (11), the first summation is extended over all triangles of the discrete domain $\hat{\Omega}$ having the vertex v in common. When using multigrid, the residual computed on the coarser level l has to be corrected by means of the relative local truncation error, $(\tau_{l+1}^l/S)_v$, so that a second condition is necessary to ensure conservation on the composite grid, namely,

$$\sum_{v \in \Omega^{l+1}} R_v^{\Omega^{l+1}} - \sum_{v \in \Omega_f^l} \left(R_v^{\Omega_f^l} + \left(\tau_{l+1}^l\right)_v \right) = 0 \quad \text{or} \quad \mathcal{O}(h^2) \qquad (12)$$

Equation (10), combined with Eq. (12), provides the following condition:

$$\sum_{v \in \Omega_f^l} \left(\tau_{l+1}^l\right)_v = 0 \quad \text{or} \quad \mathcal{O}(h^2) \qquad (13)$$

which ensures that no spurious source terms are introduced at level l. Equation (13) can be satisfied by choosing the residual collection operator properly: Fig. 2 provides a sketch of the contributions of each node at level $l + 1$ to the residual collection at the coarser-level nodes, denoted by dots. For example, the contribution of the node $(2i - 1, 2j)$ to the residual collection at the node (i, j) is $C_{l+1}^l[R_{2i-1,2j}^{\Omega^{l+1}}] = 1/2 \, R_{2i-1,2j}^{\Omega^{l+1}}$. Just as in the standard FAS cycle, the coarse grid correction consists in solving the following equation on level l:

$$q_t^l = \mathrm{res}(q^l) + r^l/S \qquad (14)$$

where the index v has been omitted for simplicity. In Eq. (14), the source term r^l/S corresponds to the relative local truncation error on the refined part of the grid l, whereas it is always null on the composite grid,

$$r^l = \begin{cases} 0 & \text{on } \Omega_c^l \\ \tau_{l+1}^l = C_{l+1}^l\left[R^{\Omega^{l+1}} + r^{l+1}\right] - R^{\Omega_f^l} & \text{on } \Omega_f^l \end{cases} \quad (15)$$

The correction of the solution in Ω_f^l is then prolongated bilinearly and added to the solution at the nodes of Ω^{l+1}; since the same operator is used for the interpolation of both the solution and the correction, the flow variables at the green points need to be interpolated only once, namely, in the nested iteration, so that no special treatment is required in the FAS cycle.

Concerning the local refinement strategy, the undivided pressure difference has been used as the sensor that detects whether a cell must be refined or not. The percentage of cells to be refined on the composite grid is assigned by the user, the threshold value being automatically computed using a subdivision of cells into classes.[5]

IV. Boundary Conditions

Standard characteristic boundary conditions are imposed at subsonic-inlet gridpoints, where the total enthalpy, entropy, and flow angle are specified and at subsonic-outlet gridpoints, where the pressure is prescribed.

Three different wall boundary conditions are considered in this paper. Standard characteristic conditions have been used at first to impose that the velocity component normal to the solid wall be zero at wall gridpoints. Second, the method proposed in Ref. 8, which minimizes the numerical entropy generation, has been extended to the present cell-vertex space discretization. One row of auxiliary cells is used at the wall, and the state at each mirror-image node is computed by imposing ISRE and no injection at each node of the solid boundary. With reference to the boundary depicted in Fig. 3, the ISRE conditions are discretized as follows:

$$H_{i,0} = H_{i,2} \qquad s_{i,0} = s_{i,2}$$

$$\left(\frac{\Delta p}{\Delta n}\right)_{i,1} = \left(\frac{\rho}{R}u_t^2\right)_{i,1} \quad (16)$$

where H is the total enthalpy, s is the entropy, R is the local radius of curvature of the wall, u_t is the tangential velocity component, and $\Delta p/\Delta n$ is computed using central differences, namely,

$$\left(\frac{\Delta p}{\Delta n}\right)_{i,1} = \frac{p_{i,2} - p_{i,0}}{2\Delta\eta}\frac{\partial\eta}{\partial n} + \frac{p_{i+1,1} - p_{i-1,1}}{2\Delta\xi}\frac{\partial\xi}{\partial n}$$

$$(\Delta\xi = \Delta\eta = 1) \quad (17)$$

For the finite volume flux difference splitting method employed in Ref. 8, the no-injection condition consists in setting the Roe-averaged normal velocity component at the solid interface to zero. In such a way, the normal velocity component at each auxiliary cell can be computed independently of the surrounding ones. On the contrary, in the case of the present cell-vertex residual distribution approach, the normal velocity components at the mirror points have to be chosen so that the no-injection condition,

$$(\boldsymbol{u} \cdot \boldsymbol{n})_{i,1} = 0 \quad (18)$$

be satisfied after the residual distribution. Therefore, the no-injection condition does involve up to three mirror-image points, resulting in a nonlinear tridiagonal system that can be solved by means of a Newton iteration and the Thomas algorithm. Finally, a simplified ISRE approach is employed that avoids such an implicit procedure: the normal velocity components at the auxiliary nodes are mirrored with respect to the wall, namely,

$$(\boldsymbol{u} \cdot \boldsymbol{n})_{i,0} = -(\boldsymbol{u} \cdot \boldsymbol{n})_{i,2} \quad (19)$$

Indeed, this condition, together with Eqs. (16) and (17), does not guarantee the vanishing of the velocity component normal to the wall
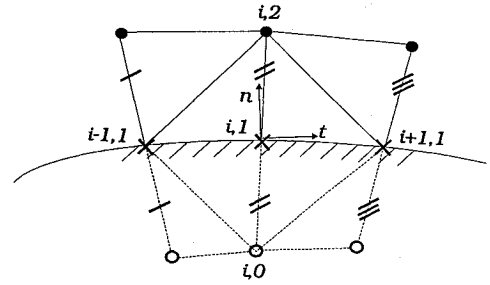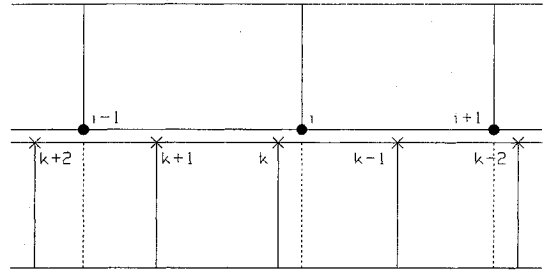

Fig. 3 Solid boundary treatment.

Fig. 4 Grid configuration on the branch cut.

at the boundary nodes. Therefore, the increments of the primitive variables are evaluated by solving the following system:

$$\Delta W_1 = \Delta\rho - (\Delta p/c^2)$$
$$\Delta W_2 = n_y\Delta u - n_x\Delta v \quad (20)$$
$$\Delta W_4 = -n_x\Delta u - n_y\Delta v + (\Delta p/\rho c)$$

where ΔW_1, ΔW_2, and ΔW_4 represent the contributions received by each boundary node in the residual distribution step. It is noteworthy that Eqs. (20) represent the standard characteristic wall boundary conditions if ΔW_1, ΔW_2, and ΔW_4 are computed without using the contributions coming from the auxiliary cells.

Concerning the treatment of the periodicity conditions on periodic grids, no particular attention is needed due to the compact space discretization and to the explicit time integration of the method. For the case of high-turning cascades, however, periodic C grids turn out to be highly skewed, so that the spatial accuracy of the solution deteriorates significantly. This problem can be cured, as proposed in Ref. 13, by abandoning the spatial coincidence between the points on the branch cut. In this way, an improved distribution of the nodes on the blade profile is obtained, which provides a reduced grid skewness. On the other hand, a particular treatment is needed for the points on the branch cut. As sketched in Fig. 4, it is possible to distinguish a coarser and a finer discretization on the two sides of the branch cut. The latter one, referred to as $\tilde{\Omega}^{l+1}$, can be thought of as a one-dimensional refinement of the coarser cells of $\tilde{\Omega}_f^l$, denoted by dashed lines in Fig. 4, which match the cells of $\tilde{\Omega}_c^l$ on the opposite side of the branch cut. The nodes $k-1$, k, and $k+1$ on the finer edge e^{l+1}, denoted by crosses in Fig. 4, are treated as green points: the corresponding states are interpolated linearly from the values at the nodes $i-1$, i, and $i+1$ of the coarser edge e^l. Following the approach described in the preceding section, the incomplete contributions of the cells of $\tilde{\Omega}^{l+1}$ to the residuals in $k-1$, k, and $k+1$ are collected at the node i of the fictitious coarser level $\tilde{\Omega}_f^l$,

$$r^l = \tau_{l+1}^l = C_{l+1}^l\left[R^{\tilde{\Omega}^{l+1}}\right] - R^{\tilde{\Omega}_f^l} \quad (21)$$

Combining Eqs. (21) and (14), the contributions $R^{\tilde{\Omega}_f^l}$ of the cells on the fictitious coarser level drop out. The residual at the node i is finally reconstructed as the sum of the contributions $R^{\tilde{\Omega}_c^l}$ and of a full-weighting collection (with weights proportional to the inverse of the distances) of the contributions $R^{\tilde{\Omega}^{l+1}}$ to the nodes $k-1$, k, and $k+1$:

$$\text{res}(q) = 1/S\left\{C_{l+1}^l\left[R^{\tilde{\Omega}^{l+1}}\right] + R^{\tilde{\Omega}_c^l}\right\} \quad (22)$$

This approach guarantees conservation. In fact, integrating along the branch cut one has

$$\int_{e^{l+1}} \mathcal{F} \cdot n \, ds - \int_{e^l} \mathcal{F} \cdot n \, ds = \mathcal{O}(h^2) \tag{23}$$

thanks to the linear variation of the data on the edges of each cell; also, from the correct choice of the collection operator, it follows that

$$\sum_{i \in e^l} r_i^l = \mathcal{O}(h^2) \tag{24}$$

which, like Eq. (13), guarantees that no spurious source terms are introduced. It is noteworthy that this technique can handle patched grids within the context of any cell-vertex residual distribution scheme and allows the use of both the multigrid and local refinement strategies, in a straightforward manner.

V.   Results

Transonic flow through a cascade of NACA 0012 airfoils with pitch-to-chord ratio equal to 3.6, isentropic outlet Mach number $M_{2,is} = 0.8$, and incidence angle $i = 1$ deg has been considered first to assess the influence of the three solid boundary treatments on the accuracy of the solution. Figures 5 and 6 provide the surface Mach number distributions obtained using three standard C grids with 96 × 16, 192 × 32, and 384 × 64 quad cells, respectively. The entire distribution is given for the suction side, whereas a blow up of the shock region is reported for the pressure side. The lines refer to the exact and simplified ISRE approaches (which always
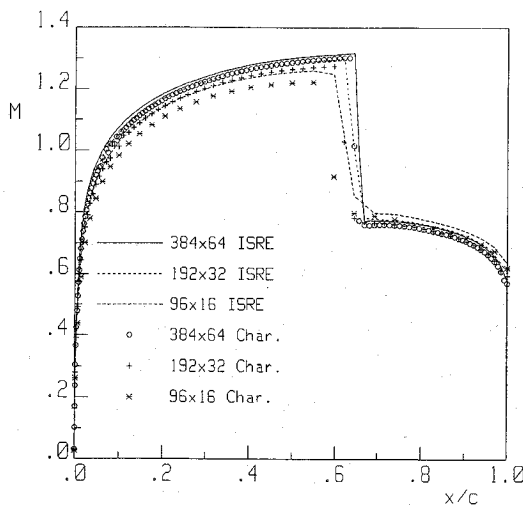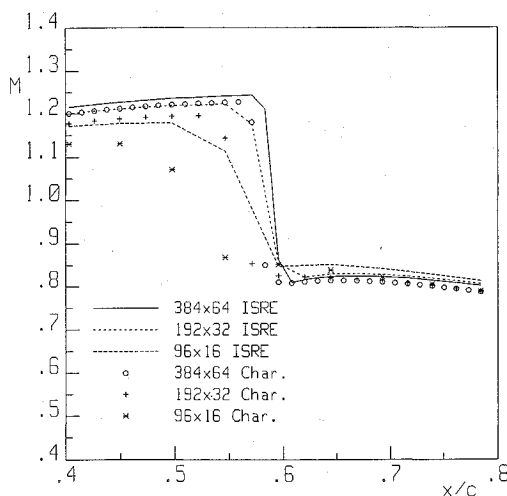
a)

b)

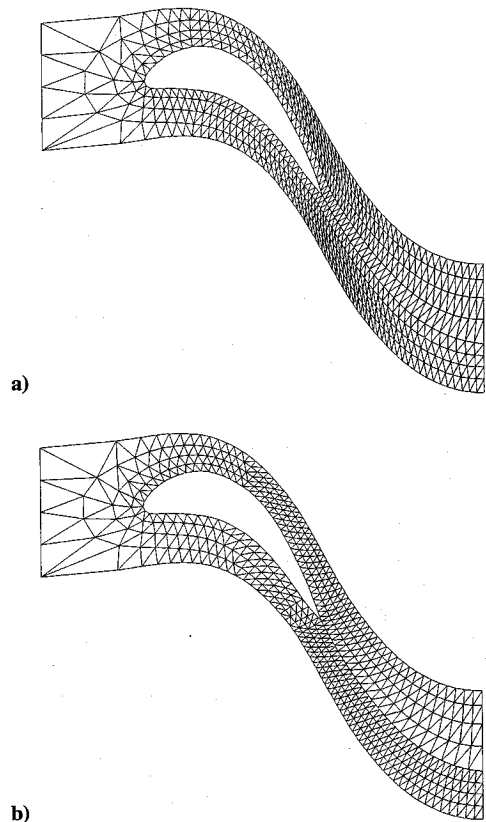**Fig. 7   Standard grid with 128×4 quad cells: a) periodic and b) nonperiodic.**

coincide within plotting accuracy), whereas the symbols refer to the characteristic solid wall boundary conditions. It is clearly apparent that the ISRE treatments allow the attainment of the same accuracy as the standard boundary conditions with one-fourth of the computational cells.

Transonic inviscid flow through a cascade of gas turbine rotor blades (VKI LS-59) with $M_{2,is} = 1$ has been then computed to validate the patched-grid treatment as well as the adaptive grid-refinement strategy. The blade profile has been modified at the trailing edge by adding an artificial wedge in order to account for the presence of the recirculation zone, which cannot be predicted by the present inviscid formulation; see also Ref. 13. Periodic and nonperiodic C grids with 256 × 8 and 512 × 16 quad cells have been used in the present computations. The 128 × 4 coarser level grids used in the multigrid approach are given in Figs. 7a and 7b. The reduced skewness of the nonperiodic grid is apparent, especially in the aftregion of the cascade. The Mach number contours obtained on the 256 × 8 periodic and nonperiodic grids are shown in Figs. 8a and 8b, respectively. The difference in the solution accuracy for this severe case is remarkable: the solution on the nonperiodic grid provides a clear description of the throat shock system and of the suction side trailing-edge shock, whereas these important features are missed almost completely by the periodic-grid solution. In order to better assess the accuracy of the solutions, the surface Mach number distributions obtained on all four grids are shown in Fig. 9. The two nonperiodic grid solutions are very close to each other, and grid convergence is practically achieved going from the 256 × 8 grid to the 512 × 16 grid. On the other hand, the periodic-grid solutions differ much more significantly, and even the finer grid solution considerably underestimates the strength of the shock.

This very severe flow situation has been employed to validate the adaptive grid-refinement strategy. Two local refinement cycles have been implemented starting from the nonperiodic 128 × 4 grid of Fig. 7b. Figure 10 shows the resulting composite grid with 5132 quad cells and the corresponding Mach number contours. The suction side trailing-edge shock maintains its orientation when crossing the branch cut, which demonstrates that the proposed patched-grid
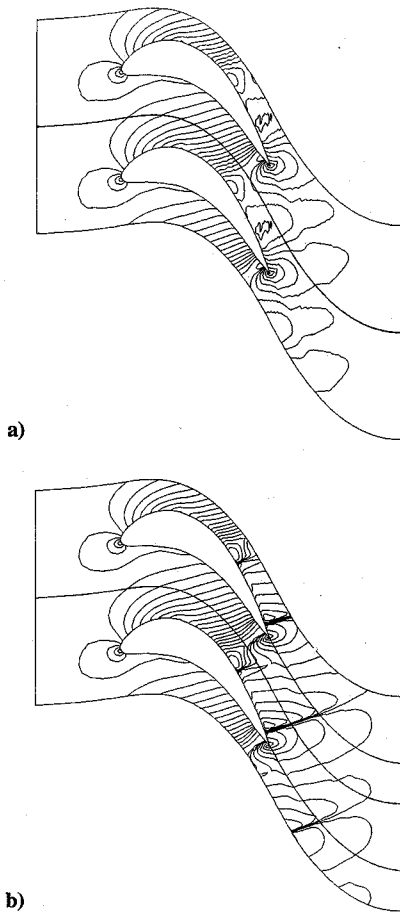

Fig. 5   Mach number distributions on the suction side.

Fig. 6   Mach number distributions on the pressure side; blow up of the shock region.

a)

b)

Fig. 8 Mach number contours (ΔM = 0.05) on standard 256 × 8 grids: a) periodic and b) nonperiodic.
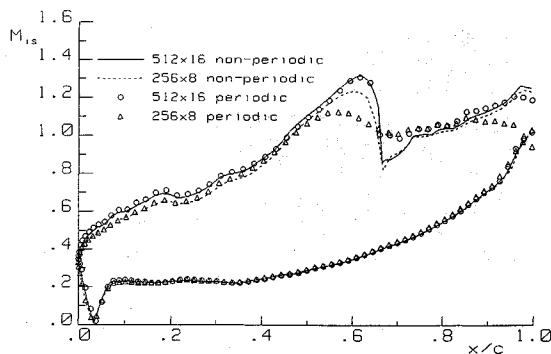
Fig. 9 Surface isentropic Mach number distributions on standard grids.

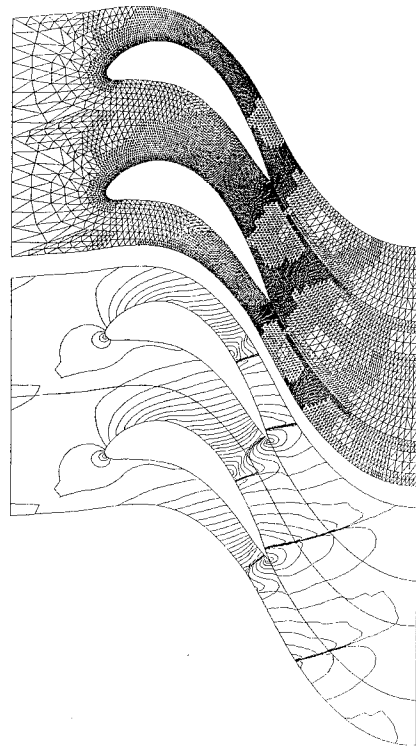**Fig. 10** Composite grid and Mach number contours (ΔM = 0.05).
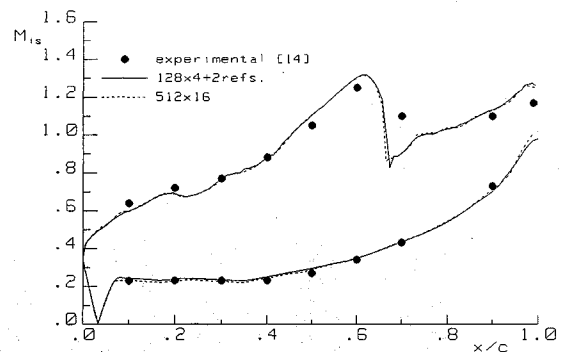
Fig. 11 Surface isentropic Mach number distributions.

Fig. 12 Convergence histories.

treatment is indeed conservative. Figure 11 provides the surface Mach number distributions for both the composite grid and the 512 × 16 standard one; the experimental results of Ref. 14 are also shown for comparison. The two numerical solutions practically coincide and agree well with the experimental data in the region where viscous effects are not important. The discrepancy in the rear part of the suction side is due to the shock/boundary-layer interaction phenomenon, which is obviously missed by the present inviscid analysis; see also Refs. 13 and 15. In order to assess the efficiency of the multigrid solution-adaptive refinement approach, the convergence histories of the composite grid (CG), single grid (SG), and four-level multigrid (MG4) calculations are presented in Fig. 12. The logarithm of the L_1 norm of the residual of the mass conservation equation is plotted vs the work, one work unit being one residual calculation on the finest grid level. A remarkable multigrid efficiency is obtained going from the single-grid to the multigrid approach. Furthermore, the work for the multigrid calculations on
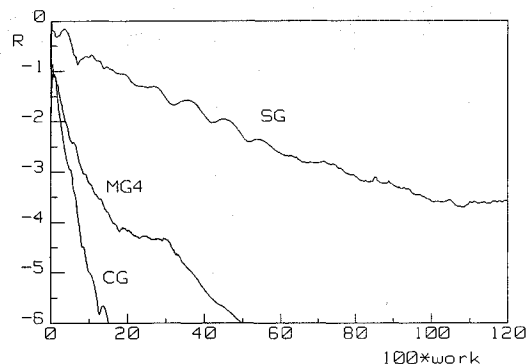
the composite and standard grids are about proportional to the total number of gridpoints employed. The efficiency and power of the proposed adaptive refinement are, thus, clearly demonstrated.

VI. Conclusions

A solution-adaptive grid-refinement procedure has been developed for an efficient multigrid strategy applied to solve two-dimensional steady inviscid flows using a multidimensional upwind cell-vertex residual distribution scheme. A very accurate treatment of solid wall boundary conditions and a general approach for

guaranteeing conservation on patched grids have been implemented and validated vs well-documented transonic cascade flows. The proposed adaptive multigrid method is shown to be very efficient and sufficiently accurate vs very complex transonic cascade flows.

Acknowledgments

References

[1]Roe, P. L., "Discrete Models for the Numerical Analysis of Time-Dependent Multidimensional Gas Dynamics," *Journal of Computational Physics*, Vol. 63, 1986, pp. 458–476.

[2]Deconinck, H., Hirsch, C., and Peuteman, J., "Characteristic Decomposition Methods for the Multidimensional Euler Equations," *Lecture Notes in Physics*, Vol. 264, 1986, pp. 216–221.

[3]Struijs, R., Deconinck, H., and Roe, P. L., "Fluctuation Splitting Schemes for the 2D Euler Equations," *Computational Fluid Dynamics*, von Kármán Inst., VKI LS 1991–01, Belgium, 1991.

[4]De Palma, P., Deconinck, H., and Struijs, R., "Investigation of Roe's 2D Wave Decomposition Models for the Euler Equations," von Kármán Inst., TN-172, Belgium, 1990.

[5]Catalano, L. A., De Palma, P., and Pascazio, G., "A Multi-Dimensional Solution Adaptive Multigrid Solver for the Euler Equations," *Lecture Notes in Physics*, Vol. 414, Springer–Verlag, Berlin, 1993, pp. 90–94.

[6]Deconinck, H., Struijs, R., Paillère, H., Catalano, L. A., De Palma, P., Napolitano, M., and Pascazio, G., "Development of Cell-Vertex Multidimensional Upwind Solvers for the Compressible Flow Equations," Centrum voor Wiskunde en Informatica, Amsterdam, *CWI-Quarterly*, Vol. 6, No. 1, 1993, pp. 1–28.

[7]Catalano, L. A., and Deconinck, H., "Two-Dimensional Optimization of Smoothing Properties of Multistage Schemes Applied to Hyperbolic Equations," von Kármán Inst. TN-173, Belgium, 1990; also "Multigrid Methods: Special Topics and Applications II," GMD-Studien No. 189, GMD St. Augustin, Germany, 1991, pp. 43–55.

[8]Dadone, A., and Grossman, B., "Surface Boundary Conditions for the Numerical Solution of the Euler Equations," *AIAA Journal*, Vol. 32, No. 2, 1994, pp. 285–293.

[9]Roe, P. L., and Beard, L., "An Improved Wave Model for Multidimensional Upwinding of the Euler Equations," *Lecture Notes in Physics*, Vol. 414, Springer–Verlag, Berlin, 1993, pp. 135–139.

[10]Roe, P. L., Struijs, R., and Deconinck, H., "A Conservative Linearization of the Multidimensional Euler Equations," *Journal of Computational Physics* (to be published).

[11]Hemker, P. W., van der Maarel, H. T. M., and Everaars, C. T. H., "A Data Structure for Adaptive Multigrid Computations," Centrum voor Wiskunde en Informatica, Rept. NM-R9014, Amsterdam, 1990.

[12]Brandt, A., "Guide to Multigrid Development," *Lecture Notes in Mathematics*, Vol. 960, Springer–Verlag, Berlin, 1982, pp. 220–312.

[13]Arnone, A., Liou, M.-S., and Povinelli, L. A., "Transonic Cascade Flow Calculations Using Non-periodic C-type Grids," Computational Fluid Dynamics Symposium on Aeropropulsion, NASA Lewis Research Center, Cleveland, OH, April 1990.

[14]Kiock, R., Lethaus, F., Baines, N. C., and Sieverding, C. H., "The Transonic Flow through a Plane Turbine Cascade as Measured in Four European Wind Tunnels," *Journal of Engineering for Gas Turbines and Power*, Vol. 108, 1986, pp. 277–285.

[15]Arnone, A., and Swanson, R. C., "Navier–Stokes Solver for Turbomachinery Applications," *Journal of Turbomachinery*, Vol. 115, 1993, pp. 305–313.